Benchmark Evaluation of Hybrid Fixed-Flapping Wing Aerial Robot With Autopilot Architecture for Autonomous Outdoor Flight Operations

Diego Gayango [ID], Rafael Salmoral, Honorio Romero, Jose Manuel Carmona, Alejandro Suarez [ID], and Anibal Ollero [ID], *Fellow, IEEE*

Abstract—This letter is focused on the benchmark evaluation and comparison of the flapping and fixed wing flight modes on an hybrid platform developed for the realization of autonomous inspection operations outdoors. The platform combines the high range and endurance of fixed-wing UAVs (unmanned aerial vehicles), with the higher maneuverability and intrinsic safety of flapping wing in the interaction with humans during the hand launch and capture. A unified model of the hybrid platform is derived for both configurations following the Lagrange formulation to express the multi-body dynamics and aerodynamic forces of the flapping wing and the propellers. The proposed control scheme exploits the similarities of both flight modes in the tail actuation and in the generation of thrust either with the flapping wings or the propellers, in such a way that it can be implemented on conventional autopilots, facilitating in this way the adoption of this type of aerial platforms. To evaluate and compare the performance of both modes, a set of benchmark tests and metrics are defined, including the energy efficiency in forward flight, trajectory tracking, hand launch and capture, and accuracy in visual inspection. Experimental results in outdoors validate the developed prototype, identifying the fixed/flapping transitions, and evidencing the higher energy efficiency of the flapping wing mode compared to the fixed wing.

Index Terms—Aerial robotics applications, benchmarking, energy efficiency, fixed-wing aerial robots, flapping-wing aerial robots.

I. INTRODUCTION

THE aerial robotics field is experiencing an evolution in the development of flying platforms, from the unmanned helicopters and fixed-wing UAVs (unmanned aerial vehicles)

Fig. 1. Hybrid fixed-flapping wing aerial robot conducting an autonomous operation in outdoors consisting of following a trajectory defined by four way-points. The platform is hand launched and safely captured by a human.

employed in the 90's and early 2000 s, to the extensive use of multi-rotors from the decade of 2010 until now [1], [2], [3]. The new paradigm of developing biologically inspired UAVs that integrate perception and manipulation capabilities [4] is motivated in terms of energy efficiency and safety in close interaction with humans, leading to novel applications that benefit from the features of these platforms, like the delivery of medicines to injured people in urban areas, roads or mountains, the inspection of large infrastructures like power lines or solar farms, or the observation and study of bird species on flight. These applications demand the ability to fly long distances, more suitable for fixed-wing UAVs than for multi-rotors, as well as safety aspects due to the proximity or interaction with humans and other animals. However, one of the current challenges to be addressed with these platforms is the realization of autonomous flight operations in outdoors, as the visual inspection of farmlands depicted in Fig. 1.

A. Flapping Wing Aerial Robots

Literature review reveals an early interest in insect-size flapping wing micro air vehicles [5], [6], [7], where one of the main challenges is the fabrication of millimeter scale actuators capable of generating flapping frequencies in the range of tens or hundreds of Hz using piezoelectric, thermal, electrostatic,

or dielectric actuation principles [5]. However, in last years the focus has moved to the development of bird-scale flapping wing robots [4], [8], [9], [10], [11], also known as ornithopters, that provide a certain payload capacity [12] to integrate perception [13], perching [14], [15] and manipulation capabilities [16]. Depending on the way the flapping motion is achieved, two implementations can be identified: continuous rotation brushless motor with small reduction ratio gear stage and rod-crank mechanism [10], [12], and servo-based actuation with higher control capabilities but lower flapping frequencies [8], [17]. Reference [17] compares different features of both solutions in terms of power consumption, proposing a modular design approach that simplifies the construction of the robot.

B. Modeling and Control

The modeling and control of fixed-wing UAVs has been extensively studied in last decades [18], [19], while in last years the development of this kind of platforms has been supported by open-source autopilots [20] and simulation frameworks [21] that have contributed to the rise of UAVs for research purposes, demonstrating the stability of simple but reliable and robust PID cascade control schemes [22].

Flapping wing robots can be assimilated to multi-body aerial systems [23], [24], [25] considering the body frame and wing masses, so a Lagrange formulation can be adopted to express the dynamics in the usual compact matrix form. The derivation of the model typically consists of two parts [26]: the kinematics and dynamics of the wings and body, and the aerodynamic equations that relate the forces and moments acting on the robot due to the action of the wings [27] and tail [25]. Some aerodynamic studies have been conducted to compare the energy efficiency of both flapping and fixed wing configurations [28], [29], [30], considering different size and scaling factors.

C. Applications and Safety Issues

The possibility to conduct autonomous flight operations outdoors with the fixed-flapping wing aerial robot presented in this paper (see Fig. 1) may result of particular interest for the inspection of large infrastructures such as the power grid [31], wind and solar farms, oil and gas refineries, or for crop monitoring in extensive farmlands [32], requiring long endurance and high energy efficiency with medium flight speeds (5-10 m/s). The ability to glide in case of fault facilitates in terms of safety the integration of these platforms in urban environments or roads to monitor crowds [33], [34] or traffic conditions [35], where a multi-rotor fall might cause serious injuries to people or damages to the environment. The bio-mimetic design of the aerial robot also reduces the visual and acoustic impact when flying close to other bird species or animals [36], allowing even the close observation on flight to study avian behaviours or migratory patterns. However, when the application requires hovering or flying at very low speeds (below 1 m/s), for example in detailed visual inspection, a multi-rotor may be more suitable and efficient. Also, the performance of a properly designed fixed-wing
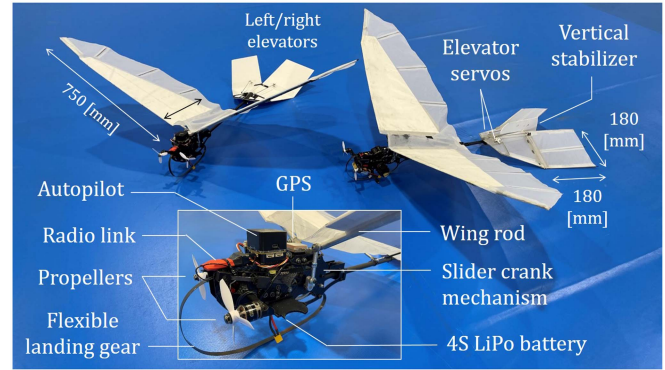

Fig. 2. Hybrid fixed-flapping wing aerial robot prototype.

UAV will be better compared to hybrid platforms when higher flight speeds (above 15 m/s) are required.

D. Main Contribution and Novelties

The main contribution of this paper is the benchmark evaluation and comparison of the fixed and flapping wing flight modes in an hybrid platform developed for autonomous outdoor operations, considering several factors such as energy efficiency, trajectory tracking, maneuverability, safety, and accuracy in visual inspection. A simplified but unified dynamic model is proposed, considering a multi-body Lagrange approach to express the equations of motion of the fixed/flapping wing platform. In order to extend the use of this kind of aerial robots, the proposed control scheme is implemented on conventional autopilots, benefiting also from reliable fixed-wing UAV controllers. Outdoor flight tests are presented to evaluate the performance of the UAV, as well as to validate the application of the aerial robot to the visual inspection of power lines.

The rest of the paper is organized as follows. Section II describes the developed platform. Section III covers the system modeling, whereas Section IV is devoted to the control architecture. Benchmarks and performance metrics of the aerial robot are defined in Section V, presenting the results in Section VI and the conclusions in Section VII.

II. DEVELOPED PLATFORM

The modeling, control, and benchmark methods described in next sections will be evaluated on the hybrid fixed-flapping wing aerial robot shown in Fig. 2. This is an evolution of the eFlap platform [12] that employs a slider-crank mechanism to generate the flapping motion from a 150 W brushless motor and a three-stage gearbox (42:1 reduction ratio), introducing the following novelties:

- Implementation of autopilot architecture employed in fixed wing UAVs [22] and multi-rotors for autonomous outdoors operations, consisting of a Cube Black controller with the Arduplane firmware and GPS receiver, facilitating the integration of a wide variety of sensors such as optical flow for estimating ground velocity.
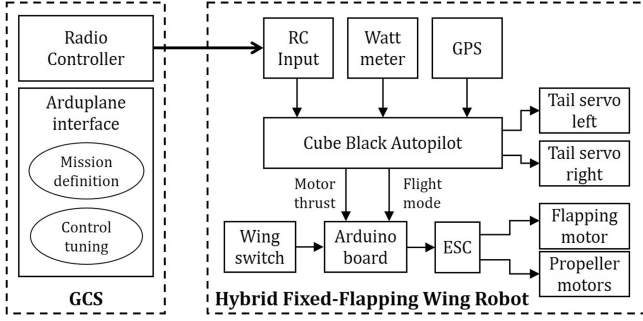
Fig. 3. Components and system architecture of the hybrid fixed-flapping wing aerial robot, including the Ground Control Station (GCS).
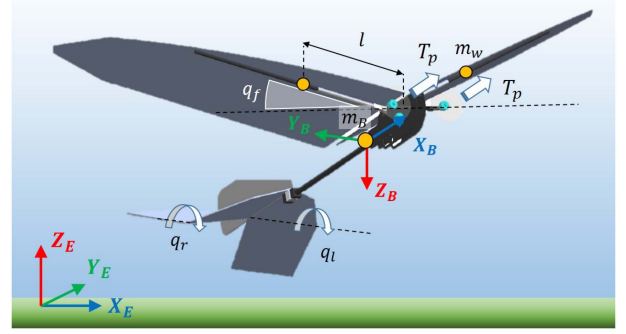

Fig. 4. Model of the fixed-flapping wing aerial robot, indicting reference frames, tail and flapping angles, thrust vectors, and body/wing masses.

- Incorporation of a pair small propellers in the front to produce thrust in fixed-wing mode and compensate the aerodynamic drag moments.
- Integration of microcontroller board and micro-switch to enable flapping-to-fixed wing transition by detecting and blocking the wings at the desired dihedral angle.
- Partial stiffening of wings/tail with polystyrene foam sheets to increase thrust in flapping mode while assimilating the aerodynamic profile to a fixed-wing UAV.
- Incorporation of a thin flexible steel curved frame at the base as landing gear to avoid frequent damages caused by the impact with the ground.

The components and architecture of the aerial robot are depicted in Fig. 3, including the Ground Control Station (GCS) from which the flight mission is defined. This is done by specifying a list of desired way-points in GPS coordinates, flight altitude and speed through the Mission Planner interface. These parameters, along with the attitude and velocity control gains tuned for both flight modes, are then transferred to the Cube Black autopilot through the WiFi data link. The platform can be controlled either manually or autonomously, allowing the on-flight commutation between fixed or flapping wing mode thanks to the Arduino board (see Section IV-C). The robot, weighting 0.93 kg, is fed by a 450 mAh 4S LiPo battery (60 grams weight), providing an approximate flight time of 7 minutes and around 1.6 km range. Note that multi-rotors of similar weight typically employ batteries with 10 times more capacity (4.500 mAh, 480 grams), providing flight times around 15 minutes.

III. Modeling

A. Kinematics and Dynamics

Two reference frames are considered in the model, as illustrated in Fig. 4: the Earth fixed frame $\{E\}$ (inertial), and the body fixed frame $\{B\}$ whose origin is located at the center of mass (CoM) of the platform fuselage, with the XYZ axes pointing in the North-East-Down directions. The position of the aerial robot in the inertial frame will be represented by $\mathbf{r_B^E} = [x, y, z]^\top$, whereas $\eta_\mathbf{B}^\mathbf{E} = [\phi, \theta, \psi]^\top$ is the orientation expressed in the roll-pitch-yaw angles. The linear and angular velocities of the platform in the body frame, estimated

from the inertial measurement unit (IMU) and GPS sensors, will be denoted by $\mathbf{v_B^B} = [u, v, w]^\top$ and $\omega_B^B = [p, q, r]^\top$, respectively. The body and inertial velocities are related as follows:

$$\dot{\mathbf{r}}_\mathbf{B}^\mathbf{E} = \mathbf{R_B^E v_B^B}; \; \dot{\eta}_\mathbf{B}^\mathbf{E} = \begin{bmatrix} 1 & 0 & -s(\theta) \\ 0 & c(\phi) & c(\theta)s(\phi) \\ 0 & -s(\phi) & c(\theta)c(\phi) \end{bmatrix}^{-1} \omega_\mathbf{B}^\mathbf{B} \quad (1)$$

where $\mathbf{R_B^E}$ is the rotation matrix, $c = cos$ and $s = sin$. The flapping angle of the wings w.r.t. the $\mathbf{X_B Y_B}$ plane is q_f, whereas q_l and q_r are the left and right rotation angles of the tail. For the fixed-wing flight mode, the flapping angle will be constant and equal to the dihedral angle, $q_f = q_0$.

The derivation of the robot dynamics relies on the similarities in the mechanical construction and aerodynamic features of fixed and flapping wing platforms, considering a unified model valid for both configurations following the Lagrangian approach for multi-body systems [23], [24], [25], [37]:

$$\frac{d}{dt}\left\{\frac{\partial\mathcal{L}}{\partial\dot{\mathbf{q}}}\right\} - \left\{\frac{\partial\mathcal{L}}{\partial\mathbf{q}}\right\} = \mathbf{\Gamma}; \; L = K - V \quad (2)$$

where L is the Lagrangian, defined as the difference between the kinetic and potential energy K and V, whereas $\mathbf{q}$ and $\mathbf{\Gamma}$ are the vectors of generalized coordinates and forces:

$$\mathbf{q} = [x, \, y, \, z, \, \phi, \, \theta, \, \psi, \, q_f]^\top \quad (3)$$

$$\mathbf{\Gamma} = [F_x, \, F_y, \, F_z, \, \tau_\phi, \, \tau_\theta, \, \tau_\psi, \, \tau_f]^\top \quad (4)$$

Here $\mathbf{\Gamma}$ includes the aerodynamic forces (thrust, lift, drag) and moments (tail actuation) acting on the center of mass of the platform, and τ_f is the torque required to produce the flapping motion. The dynamics of the tail actuators will be neglected, although the aerodynamic moments in roll, pitch, and yaw are directly controlled through the left and right tail angles, q_l and q_r.

In the computation of the kinetic and potential energy, three masses/inertias are considered [37] corresponding to the main body m_b, $\mathbf{I}_b$ and to the left/right wings m_w, $\mathbf{I}_w$, whose CoM is at distance l w.r.t. the $\mathbf{X_B}$ axis (see Fig. 4):

$$K = \frac{1}{2}\left(m_B\|\dot{\mathbf{r}}_\mathbf{B}^\mathbf{E}\|^2 + \omega_B^\top \mathbf{I}_b\omega_B^\top\right.$$

$$+ \sum_{k=1}^{2} \left(m_w \| \dot{\mathbf{r}}_{w,k}^{\mathbf{E}} \|^2 + \boldsymbol{\omega}_{w,k}^{\top} \mathbf{I}_w \boldsymbol{\omega}_{w,k}^{\top} \right) \right) \qquad (5)$$

Here $\boldsymbol{\omega}_B$ is the angular speed of the base in the inertial frame, whereas $\mathbf{r}_{w,k}$ and $\boldsymbol{\omega}_{w,k}$ are the position and angular speed of the center of mass of the left and right wings ($k = \{l, r\}$), respectively. The wing CoM position in the inertia frame is given by:

$$\mathbf{r}_{w,k}^{\mathbf{E}} = \mathbf{R}_{\mathbf{B}}^{\mathbf{E}}(\boldsymbol{\eta}) \begin{bmatrix} 0 \\ (-1)^k \, l \, cos(q_f) \\ l \, sin(q_f) \end{bmatrix} + \mathbf{r}_{\mathbf{B}} \qquad (6)$$

The potential energy is simply:

$$V = g \, \mathbf{e_3}^{\top} \left(m_b \mathbf{r}_{\mathbf{B}}^{\mathbf{E}} + m_w (\mathbf{r}_{w,l}^{\mathbf{E}} + \mathbf{r}_{w,r}^{\mathbf{E}}) \right) \qquad (7)$$

where g is the gravity constant, and $\mathbf{e_3} = [0, 0, 1]^{\top}$. The equations of motion in the compact matrix form are then:

$$\mathbf{M}(\mathbf{q})\ddot{\mathbf{q}} + \mathbf{C}(\mathbf{q}, \dot{\mathbf{q}})\dot{\mathbf{q}} + \mathbf{G}(\mathbf{q}) = \boldsymbol{\Gamma} \qquad (8)$$

Here $\mathbf{M} \in \mathbb{R}^{7 \times 7}$ is the generalized inertia matrix, $\mathbf{C} \in \mathbb{R}^{7 \times 7}$ represents the centrifugal and Coriolis terms, and $\mathbf{G} \in \mathbb{R}^{7}$ is the gravity vector. Note that, similarly as occurs with aerial robots equipped with robotic manipulators [3], the motion of the wing masses will be dynamically coupled with the vehicle attitude in the flapping wing mode.

B. Aerodynamics

The vector of generalized forces defined in (4) contains the aerodynamic forces and moments [25] induced over the platform CoM due to the the following control signals:

- The torque τ_f that produces a flapping frequency $\dot{q}_f$ (around 5 Hz, identified from the accelerometer data) to generate thrust and lift [26], [27].
- The left and right elevator angles, q_l and q_r, that induce the roll, pitch, and yaw moments on the base [18], [19].
- The thrust produced by the left and right propellers of the fixed-wing configuration, T_p, assumed to have the same magnitude.

The forces and moments generated by these control signals are derived from the aerodynamic equations detailed in [18], [19]. The flight mode will be represented by the binary variable δ, such that $\delta = 0$ corresponds to the fixed-wing mode, and $\delta = 1$ is for the flapping-wing mode (the transition between both flight modes will be addressed in next section and identified experimentally in Section VI). Therefore, taking into account the thrust and lift force models considered in [25], [37], [38]:

$$T = 2 \, T_p \, (1 - \delta) + \delta \int_A C_D(\alpha) \rho v_w^2 \, sin(\theta) \, dA \qquad (9)$$

where T_p is the propeller thrust, C_D is the aerodynamic drag coefficient, α is the angle of attack, ρ is the air density, and v_w is the wing velocity, which depends on the flapping frequency $\dot{q}_f$ and the geometry of the wing since the integral is computed over its area A. Coefficient C_D can be determined experimentally in wind tunnel [11] measuring the wrenches for a given air speed
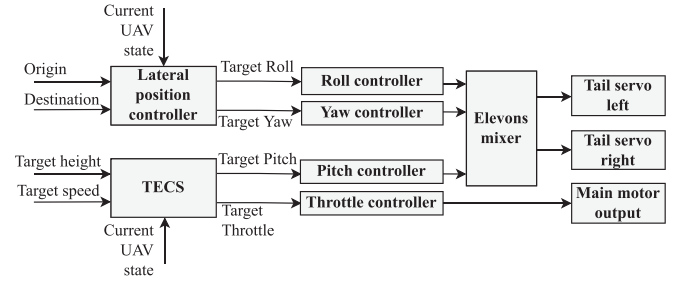

Fig. 5. Control architecture of the hybrid fixed-flapping wing robot.

and density, or numerically using computational fluid dynamics (CFD) models [39]. The autopilot will generate a commanded thrust (see section IV-A) to achieve constant velocity compensating several aerodynamic effects, including wind perturbations.

IV. CONTROL

A. Fixed Wing UAV Control

The proposed control architecture of the platform takes benefit of the ArduPlane implementation of fixed-wing UAV controllers. The adoption of standard open-source autopilots [40], widely used with multi-rotors, facilitates significantly the development of fixed-flapping wing platforms, contributing consequently to extend their use.

The UAV trajectory is controlled in a two-layer scheme, as depicted in Fig. 5. On the one hand, a lateral controller is used to navigate between way-points, taking as input the initial and reference positions along with the current state of the vehicle, obtained from an Extended Kalman Filter (EKF) that integrates the IMU, barometer, and GPS measurements, giving as output the reference signals for the low level roll-yaw controllers, described in [41]. On the other hand, to achieve the desired flight speed v and height h, the Total Energy Control System (TECS) computes the commanded thrust T_C and pitch θ_C from the mechanical energy of the vehicle given by (5) and (7), as detailed in [42]:

$$T_C = \left(K_{TP} + \frac{K_{TI}}{s} \right) \left(\gamma_e + \frac{\dot{V}_e}{g} \right) \qquad (10)$$

$$\theta_C = \left(K_{\theta P} + \frac{K_{\theta I}}{s} \right) \left(\frac{\dot{V}_e}{g} - \gamma_e \right) \qquad (11)$$

where K_P and K_I are proportional and integral gains of the thrust and pitch controllers, γ_e is the flight path angle error, where the path angle γ is defined as the difference between the pitch angle θ and the incidence angle α, and $\dot{V}_e$ is the rate of change of the airspeed error.

The low level roll-pitch controller of the UAV consists of a feed-forward PID cascade controller [22] that generates the control signals u_ϕ and u_θ taken as input by the elevators mixer in Fig. 5. Particularizing for the pitch angle:

$$u_\theta = (K_{\theta P}^r \theta_e + K_{\theta D}^r \dot{\theta}_e) + K_{\theta FF} \, \dot{\theta}_t, \qquad (12)$$
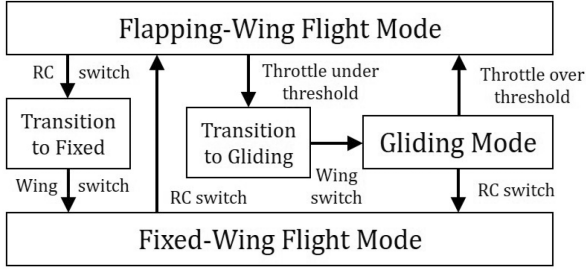
Fig. 6. State machine for switching between fixed-flapping-gliding modes.

Fig. 7. Trajectory tracking benchmark.

where $\dot{\theta}_t = K^a_{\theta P} \, \theta_e$ is the target angular rate calculated by the pitch angle controller, $\dot{\theta}_e$ the angular rate error, $K^r_{\theta P}$ the pitch rate proportional gain, $K^r_{\theta I}$ the pitch rate integral gain, $K^r_{\theta D}$ the pitch rate derivative gain, $K^r_{\theta FF}$ the feedforward pitch gain, and $K^a_{\theta P}$ the pitch angle proportional gain. The roll controller is exactly the same than pitch controller.

B. Flapping Wing UAV Control

As remarked before, the tail actuation shared in the fixed and flapping wing configurations, and the equivalence in the generation of thrust either by the propellers or by the flapping wings expressed by (9), allows the adoption of the same control architecture previously described in the flapping-wing mode without requiring hardware or software modifications of the autopilot. The only difference is that the throttle signal generated by the TECS is multiplexed by an external micro-controller (an Arduino Nano) taken as input by the Electronic Speed Controller (ESC) of the flapping motor. In order to account for the different dynamics of the fixed and flapping wing configurations, the set of controller gains is tuned for each flight mode so these are switched automatically when the pilot changes the flight mode.

C. Fixed/Flapping Wing Transition

One of the main features of this hybrid prototype is the possibility to switch between fixed and flapping wing modes on flight, allowing also the gliding by reducing the throttle under a certain threshold. In order to achieve a smooth commutation, the control logic represented in Fig. 6 has been implemented on the Arduino micro-controller that takes as input the RC channel of the flight mode (flapping/fixed) and the digital signal from the micro-switch that detects when the wings reach the fixed angle q^0. The transition from fixed wing to flapping wing is straightforward since there is no particular constraint regarding the initial condition the wings. However, the opposite transition requires to complete the flapping cycle from the instant the flight mode switches until the wings reach the fixed configuration. The same method is applied for the flapping-gliding transitions, relying on a throttle threshold for triggering the commutation. The flapping to fixed/gliding transition is triggered in the downstroke in order to prevent the counter-rotation of the wings, introducing a simple mechanism that blocks the gear in the reverse direction. In this short time (less that the flapping period, 0.2 s) the platform
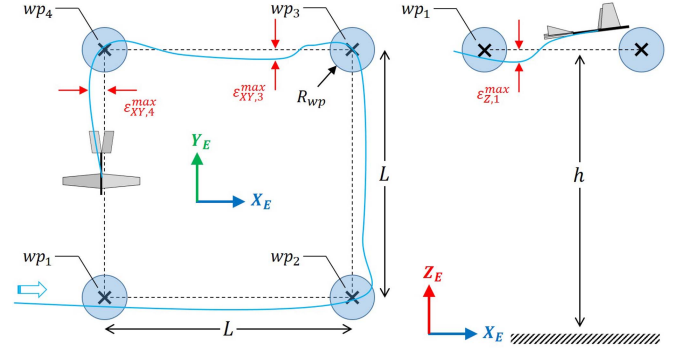
maintains the flight speed almost constant, so the attitude control is not significantly affected.

V. PERFORMANCE METRICS

A. Forward Flight Energy Consumption

Most autopilots provide measurements of the instantaneous battery voltage V and current I, which allows to obtain the instantaneous electric power P_e and therefore the energy E_e consumed in a time interval Δt from initial time t_0:

$$E_e(t_0, \Delta t) = \int_{t_0}^{t_0 + \Delta t} P_e \, dT = \int_{t_0}^{t_0 + \Delta t} V \cdot I \, dT \qquad (13)$$

During the evaluation interval $t \in [t_0, t_0 + \Delta t]$, the aerial robot should fly in steady conditions at constant nominal speed v_n, zero attitude ($\phi \approx 0, \; \theta \approx 0$), zero angular rate ($\dot{\phi} \approx 0, \; \dot{\theta} \approx 0, \; \dot{\psi} \approx 0$), and no wind. The energy performance for a given nominal speed v_n will be better as the distance traveled during the evaluation interval is higher, which leads to the definition of the metric:

$$\eta_e^{v_n} = \frac{\|\mathbf{r_B}(t_0 + \Delta t) - \mathbf{r_B}(t_0)\|}{E_e(t_0, \Delta t)} = \frac{\int_{t_0}^{t_0 + \Delta t} \|\dot{\mathbf{r}}_{\mathbf{B}}\| ds}{E_e(t_0, \Delta t)} \qquad (14)$$

where $\mathbf{r_B}$ is the position of the platform in the Earth frame. Note that this metric does not require the estimation of aerodynamic coefficients that in practice may be difficult to obtain, particularly in the case of flapping wing platforms. In case the platform is intended to carry some payload, the variation of $\eta_e^{v_n}$ with the attached mass should be indicated.

B. Trajectory Tracking

The purpose of this benchmark is to evaluate the accuracy in the trajectory tracking of the aerial platform, considering a rectangular-shape reference path [43] as the one shown in Fig. 7, consisting of four way-points separated a distance L and at height h. Way-point tracking is the usual way of defining flight missions outdoors, and the square shape of the trajectory allows to evaluate the maneuverability of the controller, instead of considering more favorable smooth trajectories. This is relevant if the operation involves flying between obstacles. Denoting as $\mathbf{r}_{wp,k} \in R^3$ the position of the k-th way-point in the Earth
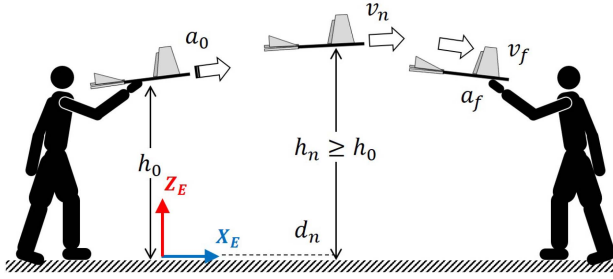
Fig. 8. Launching acceleration benchmark: hand thrown launch (left) and hand capture (right), only with flapping wing mode.

fixed frame $\{\mathbf{E}\}$, the platform crosses the way-point correctly if $\|\mathbf{r_B}(t) - \mathbf{r}_{wp,k}\| \leq R_{wp}$. The metrics of interest here are the maximum overshoot and average errors in the XY and Z axes with respect to the reference path, that is, $\varepsilon_{XY}^{\max}$, $\varepsilon_{Z}^{\max}$, $\varepsilon_{XY}^{\mathrm{avg}}$, and $\varepsilon_{Z}^{\mathrm{avg}}$, specifying the nominal flight speed v_n and attached payload.

C. Launching and Capture Acceleration

This benchmark is devoted to the evaluation of the acceleration capability with the method depicted in Fig. 8. The evaluation metric is the time t_{v_n} required by the platform to reach a nominal flight speed v_n when it is thrown by a person at height h_0 with hand acceleration a_0 with a relatively small ascending rate, so at that time the platform reaches the nominal height $h_n \geq h_0$ at distance d_n from the launching position. The flapping and gliding modes allow the safe interaction with the human in close maneuvers like the hand capture, as illustrated in Figs. 1 and 8. Here the representative metrics for evaluating the comfort in the hand capture are the final velocity v_f and peak acceleration a_f at the time the platform is grabbed.

D. Accuracy in Visual Inspection

In aerial photogrammetry, the accuracy of the acquired images is expressed through the Ground Sampling Distance (GSD), what can be defined as the distance (in cm) between two consecutive pixels measured in the world frame at a certain observation distance taken as reference. The GSD will depend on the focal length of the camera (F, in mm), the observation distance (D, in m), the camera resolution width (W in pixels) and the image sensor width (S_w in mm):

$$GSD = 100 \times (S_w \cdot D)/(F \cdot W) \tag{15}$$

Besides the benefits in terms of safety and low energy consumption, flapping-wing and hybrid platforms can achieve lower flight speeds and higher maneuverability than fixed-wing UAVs for accurate and long range inspection of vast infrastructures such as power lines or farmlands.

VI. EXPERIMENTAL RESULTS

A. Flapping-Fixed Wing Flight Transition

The goal of this experiment is to evaluate the transition on flight of the flapping-fixed wing configurations, identifying also
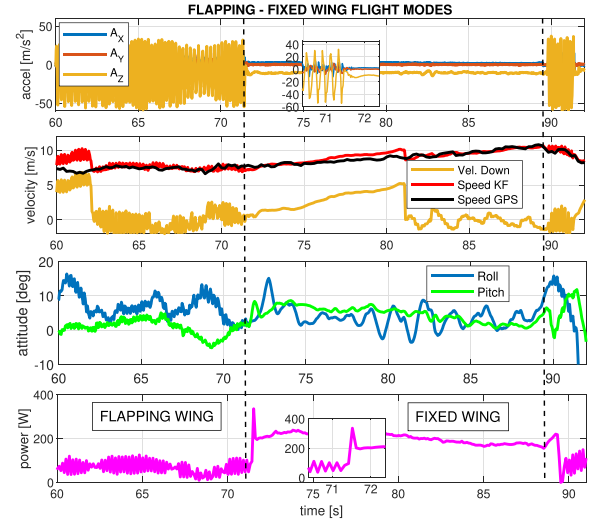

Fig. 9. Acceleration, velocity, attitude and electric power consumption of the aerial platform flying in flapping wing and fixed wing modes. The transition occurs at t = 71.38 and t = 89.49 seconds.

TABLE I
PERFORMANCE METRICS OF THE TRAJECTORY TRACKING BENCHMARK

Mode	Segment	Speed [m/s]	ε_{XY}^{max} [m]	ε_{Z}^{max} [m]
Flapping	WP2-3	4 − 6	16	1.6
Fixed	WP2-3	6 − 8	48	0.8
Flapping	WP3-4	5 − 6.8	20	1.4
Fixed	WP3-4	8 − 9.3	37	0.7

some significant differences between both modes. This outdoor test was conducted in the ATLAS Flight Test Center (Villacarrillo, Jaen). Fig. 9 represents the acceleration, velocity, orientation and electric power in a 32 seconds interval. Dashed vertical lines represent the time instants at which the flapping-fixed and fixed-flapping transitions occur. As it can be seen, the transition is smooth in the sense that there is no sudden change in the velocity or attitude. Fig. 9 also evidences a significant increase in the power consumption in the fixed wing mode (202 W average) compared to the flapping wing mode (66 W), and the reduction in the consumption from 225 to 170 W as the flight speed increases from 7.5 to 10.5 m/s in fixed mode.

B. Trajectory Tracking

An autonomous inspection mission has been carried out in a crop field in order to compare the accuracy in the trajectory tracking of both flight modes. Figs. 10 and 11 represent the execution of the experiment, consisting of tracking four way-points located at the vertices of a 150 by 100 meters rectangle, flying at a average flight speed of 5 and 8 m/s for the flapping and fixed wing modes, respectively. As it can be seen, the maneuverability of the flapping mode is higher compared w.r.t. the fixed mode as the tracking errors $\varepsilon_{XY}^{\max}$ (see Section V-B) are lower for the segments WP2-3 and WP3-4 for the given velocities, as indicated in Table I.
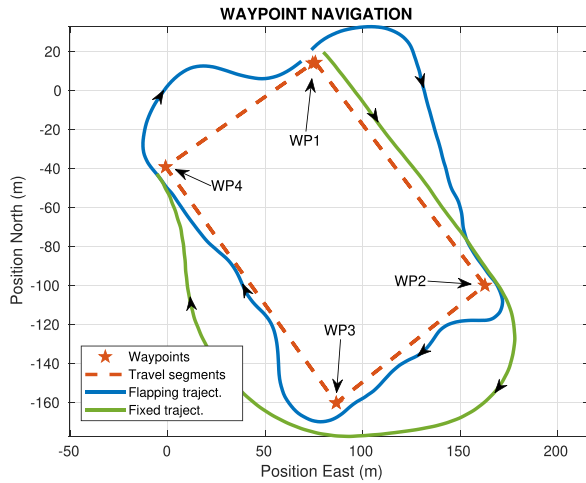
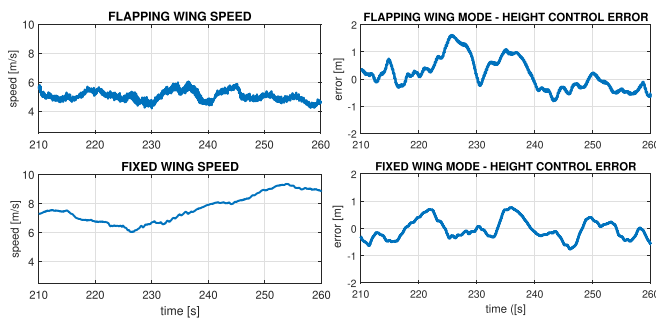Fig. 10. Flapping-wing and fixed-wing North-East trajectory tracking.

Fig. 11. Comparison of fixed-flapping wing speed and height error.

TABLE II
EVALUATION OF THE ENERGY CONSUMPTION BENCHMARK

Mode	Speed [m/s]	Energy [J]	Distance [m]	η_e [m/J]
Flapping	8 - 8.7	670	112	0.167
Fixed	6.7 - 7.5	1510	108	0.071

C. Energy Consumption Comparison

The experiment represented in Fig. 9 revealed that the hybrid platform consumed almost three times more electric power in fixed wing mode than in flapping mode. In order to evaluate the energy efficiency of both configurations, the forward flight energy consumption benchmark described in Section V-A has been applied in another autonomous outdoor flight test in which the platform is commanded to follow a linear trajectory for 15 s. Fig. 12 compares the results of consumed energy and travelled distance for both modes, indicating also the total energy. Table II summarizes the results of the benchmark, confirming the higher energy efficiency of the flapping wing mode. Note that the average power of our prototype (0.93 kg weight) is 50 W, similarly to the prototype in [11] (0.6 kg weight), whereas the power consumption of the Robird (0.73 kg) and RoboRaven (0.29 kg) is 112 W and 20 W, respectively, according to [8], [10].
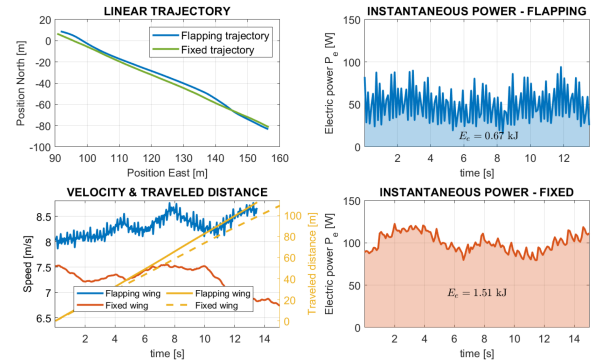

Fig. 12. Experimental evaluation of the energy efficiency benchmark. Trajectory followed in fixed and flapping wing modes (left-up), speed and traveled distance (left-down), and energy consumption (right).
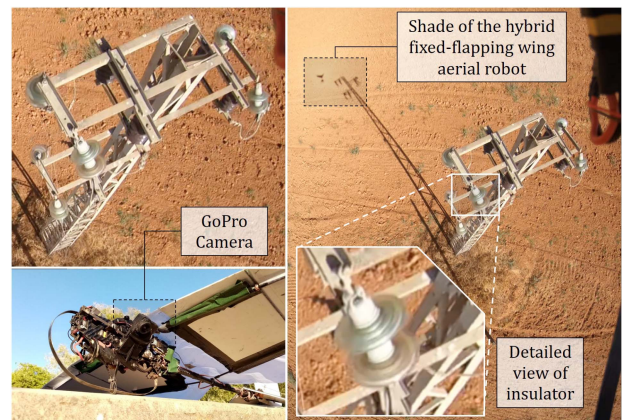

Fig. 13. General and detailed view of a power line pole obtained from the on-board camera of the hybrid fixed-flapping wing aerial robot.

D. Visual Inspection

The hybrid platform has been equipped with a GoPro Hero 7 camera to obtain accurate images and perform visual inspection of the power line transmission tower depicted in Fig. 13. The camera is mounted on on the body frame, pointing 45 degrees downwards. The accuracy in the visual inspection will be measured with the metric described in V-D, resulting in a GSD of 0.62 cm at 10 m distance. The image shown in Fig. 13 was obtained with the platform flying at a distance around 5 m from the top of the power line pole in gliding mode at 6 m/s. The higher flight speed of this platform compared to multi-rotors, along with the high accuracy of the acquired images and advanced stabilization provided by this camera, allows to detect and localize faults with greater area coverage in an autonomous way.

VII. CONCLUSIONS AND FUTURE WORK

This paper presented an hybrid fixed-flapping wing aerial robot for autonomous inspection operations that combines the benefits of both flight modes in terms of energy efficiency and safety in close interaction with humans, providing greater flight distances compared to multi-rotors. The paper proposed

a unified dynamic model for both configurations derived from the Lagrange formulation, and a control scheme relying on autopilot architecture that exploits the shared actuation of the tail and relies on well established fixed-wing controllers. A set of benchmark metrics and procedures were described, presenting experimental results outdoors that evidence the possibility to switch the flight mode smoothly while flying, and the higher maneuverability and energy efficiency of the flapping wing mode.

As future work, it is convenient to investigate novel estimation, control, and planning methods that take benefit of wind to increase energy efficiency for long-term inspection, inspired by seagulls and other birds that exploit gliding flight. Adaptive non-linear controllers should be designed for autonomous and accurate landing/perching relying on aerodynamic models that allow to conduct agile maneuvers.

References

[1] H. Shakhatreh et al., "Unmanned aerial vehicles (UAVs): A survey on civil applications and key research challenges," *IEEE Access*, vol. 7, pp. 48572–48634, 2019.

[2] M. Hamandi, F. Usai, Q. Sablé, N. Staub, M. Tognon, and A. Franchi, "Design of multirotor aerial vehicles: A taxonomy based on input allocation," *Int. J. Robot. Res.*, vol. 40, no. 8/9, pp. 1015–1044, 2021.

[3] A. Ollero, M. Tognon, A. Suarez, D. Lee, and A. Franchi, "Past, present, and future of aerial robotic manipulators," *IEEE Trans. Robot.*, vol. 38, no. 1, pp. 626–645, Feb. 2022.

[4] "ERC advanced grant GRIFFIN project (General compliant aerial robotic manipulation system integrating fixed and flapping wings to increase range and safety) webpage." [Online]. Available: https://griffin-erc-advanced-grant.eu/

[5] M. Karpelson, G.-Y. Wei, and R. J. Wood, "A review of actuation and power electronics options for flapping-wing robotic insects," in *Proc. IEEE Int. Conf. Robot. Automat.*, 2008, pp. 779–786.

[6] C. Zhang and C. Rossi, "A review of compliant transmission mechanisms for bio-inspired flapping-wing micro air vehicles," *Bioinspiration Biomimetics*, vol. 12, no. 2, 2017, Art. no. 025005.

[7] C. Chen and T. Zhang, "A review of design and fabrication of the bionic flapping wing micro air vehicles," *Micromachines*, vol. 10, no. 2, p. 144, 2019.

[8] J. Gerdes et al., "Robo raven: A flapping-wing air vehicle with highly compliant and independently controlled wings," *Soft Robot.*, vol. 1, no. 4, pp. 275–288, 2014.

[9] A. Ramezani, X. Shi, S.-J. Chung, and S. Hutchinson, "Bat bot (b2), a biologically inspired flying machine," in *Proc. IEEE Int. Conf. Robot. Automat.*, 2016, pp. 3219–3226.

[10] G. A. Folkertsma, W. Straatman, N. Nijenhuis, C. H. Venner, and S. Stramigioli, "Robird: A robotic bird of prey," *IEEE Robot. Automat. Mag.*, vol. 24, no. 3, pp. 22–29, Sep. 2017.

[11] A. Chen, B. Song, Z. Wang, D. Xue, and K. Liu, "A novel actuation strategy for an agile bioinspired FWAV performing a morphing-coupled wingbeat pattern," *IEEE Trans. Robot.*, vol. 39, no. 1, pp. 452–469, Feb. 2023.

[12] R. Zufferey et al., "Design of the high-payload flapping wing robot E-flap," *IEEE Robot. Automat. Lett.*, vol. 6, no. 2, pp. 3097–3104, Apr. 2021.

[13] J. P. Rodríguez-Gómez et al., "The GRIFFIN perception dataset: Bridging the gap between flapping-wing flight and robotic perception," *IEEE Robot. Automat. Lett.*, vol. 6, no. 2, pp. 1066–1073, Apr. 2021.

[14] A. A. Paranjape, S.-J. Chung, and J. Kim, "Novel dihedral-based control of flapping-wing aircraft with application to perching," *IEEE Trans. Robot.*, vol. 29, no. 5, pp. 1071–1084, Oct. 2013.

[15] D. Feliu-Talegon, J. Á. Acosta, and A. Ollero, "Control aware of limitations of manipulators with claw for aerial robots imitating bird's skeleton," *IEEE Robot. Automat. Lett.*, vol. 6, no. 4, pp. 6426–6433, Oct. 2021.

[16] A. Suarez, P. Grau, G. Heredia, and A. Ollero, "Winged aerial manipulation robot with dual arm and tail," *Appl. Sci.*, vol. 10, no. 14, 2020, Art. no. 4783.

[17] I. Diez-de-los Rios, A. Suarez, E. Sanchez-Laulhe, I. Armengol, and A. Ollero, "Winged aerial robot: Modular design approach," in *Proc. IEEE Int. Symp. Saf., Secur., Rescue Robot.*, 2021, pp. 190–195.

[18] R. W. Beard and T. W. McLain, *Small Unmanned Aircraft: Theory and Practice*. Princeton, NJ, USA: Princeton Univ. Press, 2012.

[19] B. L. Stevens, F. L. Lewis, and E. N. Johnson, *Aircraft Control and Simulation: Dynamics, Controls Design, and Autonomous Systems*. Hoboken, NJ, USA: Wiley, 2015.

[20] L. Meier, D. Honegger, and M. Pollefeys, "Px4: A node-based multi-threaded open source robotics framework for deeply embedded platforms," in *Proc. IEEE Int. Conf. Robot. Automat.*, 2015, pp. 6235–6240.

[21] E. Ebeid, M. Skriver, K. H. Terkildsen, K. Jensen, and U. P. Schultz, "A survey of open-source UAV flight controllers and flight simulators," *Microprocessors Microsystems*, vol. 61, pp. 11–20, 2018.

[22] S. Baldi, S. Roy, K. Yang, and D. Liu, "An underactuated control system design for adaptive autopilot of fixed-wing drones," *IEEE/ASME Trans. Mechatron.*, vol. 27, no. 5, pp. 4045–4056, Oct. 2022.

[23] J. A. Grauer and J. E. Hubbard Jr, "Multibody model of an ornithopter," *J. Guid., Control, Dyn.*, vol. 32, no. 5, pp. 1675–1679, 2009.

[24] C. T. Orlowski and A. R. Girard, "Dynamics, stability, and control analyses of flapping wing micro-air vehicles," *Prog. Aerosp. Sci.*, vol. 51, pp. 18–30, 2012.

[25] J. Hoff, U. Syed, A. Ramezani, and S. Hutchinson, "Trajectory planning for a bat-like flapping wing robot," in *Proc. IEEE/RSJ Int. Conf. Intell. Robots Syst.*, 2019, pp. 6800–6805.

[26] H. E. Taha, M. R. Hajj, and A. H. Nayfeh, "Flight dynamics and control of flapping-wing MAVs: A review," *Nonlinear Dyn.*, vol. 70, no. 2, pp. 907–939, 2012.

[27] M. F. Platzer, K. D. Jones, J. Young, and J. C. Lai, "Flapping wing aerodynamics: Progress and challenges," *AIAA J.*, vol. 46, no. 9, pp. 2136–2149, 2008.

[28] T. J. Mueller, *Fixed and Flapping Wing Aerodynamics for Micro Air Vehicle Applications*. Reston, VA, USA: AIAA, 2001.

[29] U. Pesavento and Z. J. Wang, "Flapping wing flight can save aerodynamic power compared to steady flight," *Phys. Rev. Lett.*, vol. 103, no. 11, 2009, Art. no. 118102.

[30] G. Sachs, "Comparison of power requirements: Flapping vs. fixed wing vehicles," *Aerospace*, vol. 3, no. 4, 2016, Art. no. 31.

[31] G. Silano, T. Baca, R. Penicka, D. Liuzza, and M. Saska, "Power line inspection tasks with multi-aerial robot systems via signal temporal logic specifications," *IEEE Robot. Automat. Lett.*, vol. 6, no. 2, pp. 4169–4176, Apr. 2021.

[32] P. Lottes, R. Khanna, J. Pfeifer, R. Siegwart, and C. Stachniss, "Uav-based crop and weed classification for smart farming," in *Proc. IEEE Int. Conf. Robot. Automat.*, 2017, pp. 3024–3031.

[33] R. S. de Moraes and E. P. de Freitas, "Multi-UAV based crowd monitoring system," *IEEE Trans. Aerosp. Electron. Syst.*, vol. 56, no. 2, pp. 1332–1345, Apr. 2020.

[34] P. Pannozzi, K. P. Valavanis, M. J. Rutherford, G. Guglieri, M. Scanavino, and F. Quagliotti, "Urban monitoring of smart communities using UAS," in *Proc. Int. Conf. Unmanned Aircr. Syst.*, 2019, pp. 866–873.

[35] H. Huang, A. V. Savkin, and C. Huang, "Decentralized autonomous navigation of a UAV network for road traffic monitoring," *IEEE Trans. Aerosp. Electron. Syst.*, vol. 57, no. 4, pp. 2558–2564, Aug. 2021.

[36] M. M. Nowak, K. Dziób, and P. Bogawski, "Unmanned aerial vehicles (UAVs) in environmental biology: A review," *Eur. J. Ecol.*, vol. 4, no. 2, pp. 56–74, 2018.

[37] B. E. Wissa, K. O. Elshafei, and A. A. El-Badawy, "Lyapunov-based control and trajectory tracking of a 6-dof flapping wing micro aerial vehicle," *Nonlinear Dyn.*, vol. 99, no. 4, pp. 2919–2938, 2020.

[38] D. Mueller, H. Bruck, and S. Gupta, "Measurement of thrust and lift forces associated with drag of compliant flapping wing for micro air vehicles using a new test stand design," *Exp. Mechanics*, vol. 50, no. 6, pp. 725–735, 2010.

[39] S. P. Sane and M. H. Dickinson, "The control of flight force by a flapping wing: Lift and drag production," *J. Exp. Biol.*, vol. 204, no. 15, pp. 2607–2626, 2001.

[40] "ArduPilot open source flight controller documentation." [Online]. Available: https://ardupilot.org/ardupilot/

[41] S. Park, J. Deyst, and J. How, "A new nonlinear guidance logic for trajectory tracking," in *Proc. AIAA Guid., Navigation, Control Conf. Exhibit*, 2004, Art. no. 4900.

[42] A. Lambregts, "Vertical flight path and speed control autopilot design using total energy principles," in *Proc. Guid. Control Conf.*, 1983, Art. no. 2239.

[43] Y. Kang and J. K. Hedrick, "Linear tracking for a fixed-wing UAV using nonlinear model predictive control," *IEEE Trans. Control Syst. Technol.*, vol. 17, no. 5, pp. 1202–1210, Sep. 2009.